

1      **Constraining Non-Methane VOC Emissions with TROPOMI HCHO**  
2      **observations: Impact on Summertime Ozone Simulation in**  
3      **August 2022 in China**

4      **~~Constraint of non-methane volatile organic compound emissions with~~**  
5      **~~TROPOMI HCHO observations and its impact on summertime~~**  
6      **~~surface ozone simulation over China~~**

7  
8      Shuzhuang Feng<sup>1</sup>, Fei Jiang<sup>1,2,5\*</sup>, Tianlu Qian<sup>3</sup>, Nan Wang<sup>4</sup>, Mengwei Jia<sup>1</sup>, Songci  
9      Zheng<sup>1</sup>, Jiansong Chen<sup>6</sup>, Fang Ying<sup>6</sup>, Weimin Ju<sup>1,2</sup>

10  
11     <sup>1</sup> *Jiangsu Provincial Key Laboratory of Geographic Information Science and*  
12     *Technology, International Institute for Earth System Science, Nanjing University,*  
13     *Nanjing, 210023, China*

14     <sup>2</sup> *Jiangsu Center for Collaborative Innovation in Geographical Information Resource*  
15     *Development and Application, Nanjing, 210023, China*

16     <sup>3</sup> *School of Internet of Things, Nanjing University of Posts and Telecommunications,*  
17     *Nanjing, 210042, China*

18     <sup>4</sup> *College of Carbon Neutrality Future Technology, Sichuan University, Chengdu,*  
19     *610207, China*

20     <sup>5</sup> *Frontiers Science Center for Critical Earth Material Cycling, Nanjing University,*  
21     *Nanjing, 210023, China*

22     <sup>6</sup> *Hangzhou Municipal Ecology and Environment Bureau, Hangzhou, 310020, China*

23  
24  
25  
26  

---

\* Corresponding author: Tel.: +86-25-83597077; Fax: +86-25-83592288; E-mail address: jiangf@nju.edu.cn

27 **Abstract**

28 Non-methane volatile organic compounds (NMVOC), serving as crucial precursors  
29 of  $O_3$ , have a significant impact on atmospheric oxidative capacity and  $O_3$  formation.  
30 However, both anthropogenic and biogenic NMVOC emissions remain subject to  
31 considerable uncertainty. Here, we extended the Regional multi-Air Pollutant  
32 Assimilation System (RAPAS) with the EnKF algorithm to optimize NMVOC  
33 emissions in China [in August 2022](#) by assimilating TROPOMI HCHO retrievals.  
34 We also simultaneously optimize  $NO_x$  emissions by assimilating in-situ  $NO_2$   
35 observations to address the chemical feedback among VOC- $NO_x$ - $O_3$ . Furthermore,  
36 a process-based analysis was employed to quantify the impact of NMVOC emission  
37 changes on various chemical reactions related to  $O_3$  formation and depletion.  
38 NMVOC emissions exhibited a substantial reduction of 50.2%, especially in [forest-rich areas of central and southern China](#) [the middle and lower reaches of the Yangtze River](#), revealing a prior overestimation of biogenic NMVOC emissions [due to extreme heatwave](#). Compared with the forecast with prior NMVOC emissions, the  
40 forecast with posterior emissions significantly improved HCHO simulations,  
41 reducing biases by 75.7%, indicating a notable decrease in posterior emission  
42 uncertainties. The forecast with posterior emissions also effectively corrected the  
43 overestimation of  $O_3$  in forecast with prior emissions, reducing biases by 49.3%.  
44 This can be primarily attributed to a significant decrease in the  $RO_2 + NO$  reaction  
45 rate and an increase in the  $NO_2 + OH$  reaction rate in the afternoon, thus limiting  $O_3$   
46 generation. Sensitivity analyses emphasized the necessity of considering both  
47 NMVOC and  $NO_x$  emissions for a comprehensive assessment of  $O_3$  chemistry. This  
48 study enhances our understanding of the effects of NMVOC emissions on  $O_3$   
49 production and can contribute to the development of effective emission reduction  
50 policies.

53  
54 **Keywords**

55 NMVOC emissions,  $O_3$  pollution, Emission inversion, HCHO column retrievals, Data  
56 assimilation

59 **1 Introduction**

60 Since the Chinese government implemented the Air Pollution Prevention and Control  
61 Action Plan in 2013, there has been a notable reduction in NO<sub>x</sub> emissions (Zheng et al.,  
62 2018). However, despite these advancements, the issue of O<sub>3</sub> pollution persists and, in  
63 certain cases, has shown signs of worsening (Ren et al., 2022). The increase in O<sub>3</sub>  
64 concentration can be attributed not only to adverse meteorological conditions but also  
65 predominantly to unbalanced joint control of non-methane volatile organic compounds  
66 (NMVOCs) and nitrogen oxides (NO<sub>x</sub>) (Li et al., 2020). NMVOCs are vital precursors  
67 of O<sub>3</sub> and have a substantial impact on the atmospheric oxidation capacity, thereby  
68 altering the lifetimes of other pollutants. Accurately quantifying NMVOC emissions  
69 holds significant importance in investigating their impact on O<sub>3</sub> chemistry and in  
70 formulating emission reduction policies.

71 Anthropogenic NMVOC emissions have traditionally been estimated using a “bottom-  
72 up” method. However, the accuracy and timeliness of these estimations face challenges  
73 owing to the scarcity of local measurements for emission factors, the incompleteness  
74 and unreliability of activity data, and the diverse range of species and technologies  
75 involved (Cao et al., 2018; Hong et al., 2017). Furthermore, uncertainties arise in  
76 model-ready NMVOC emissions due to spatial and temporal allocations using various  
77 “proxy” data for different source sectors (Li et al., 2017a). Li et al. (2021) reported  
78 substantial discrepancies among emission estimates in various studies, ranging 23% to  
79 56%. Biogenic NMVOC emissions are typically estimated using models like the Model  
80 of Emissions of Gases and Aerosols from Nature (MEGAN) (Guenther et al., 2012) and  
81 the Biogenic Emission Inventory System (BEIS) (Pierce et al., 1998). NMVOC  
82 emissions result from the multiplication of plant-specific standard emission rates by  
83 dimensionless activity factors. Nonetheless, apart from inaccuracies in the distribution  
84 of plant functional types, empirical parameterization, especially concerning responses  
85 to temperature and drought stress, can introduce substantial uncertainties (Angot et al.,  
86 2020; Seco et al., 2022; Jiang et al., 2018). Warneke et al. (2010) determined isoprene  
87 emission rates through field measurements and conducted a comparison with MEGAN  
88 and BEIS estimates, revealing a notable tendency for MEGAN to overestimate  
89 emissions, while BEIS consistently underestimated them. Similarly, Marais et al. (2014)  
90 found that MEGAN's isoprene emission estimates were 5-10 times higher than the  
91 canopy-scale flux measurements obtained from African field campaigns.

92 A top-down approach, utilizing observed data, has been developed for estimating VOCs  
93 emissions. For instance, based on aircraft and ground-based field measurements, the  
94 source-receptor relationships algorithm with Lagrangian particle dispersion model  
95 (Fang et al., 2016), mixed layer gradient techniques (Mo et al., 2020), eddy covariance  
96 flux measurements (Yuan et al., 2015), and box model (Wang et al., 2020) have been  
97 employed to complement or verify bottom-up results. However, these approaches do  
98 not comprehensively consider the complex nonlinear chemical reactions and transport  
99 processes that VOCs undergo in the atmosphere. Formaldehyde (HCHO) and glyoxal  
100 (CHOCHO) in the atmosphere serve as crucial oxidization intermediates for various  
101 VOCs (Hong et al., 2021; Liu et al., 2012). Satellite-based observations can readily  
102 detect their presence in the form of vertical column density (VCD) from space, making  
103 them widely utilized for estimating NMVOC emissions. A commonly used approach  
104 assumes that the observed HCHO/CHOCHO columns are locally linearly correlated  
105 with VOC emission rates (Palmer et al., 2006; Liu et al., 2012). However, this approach  
106 does not consider the spatial offset resulting from chemistry reactions and transport  
107 processes. Chaliyakunnel et al. (2019) conducted a Bayesian analysis to derive an  
108 optimal estimate of VOC emissions using HCHO measurements over the Indian  
109 subcontinent. Their results indicated that biogenic VOC emissions modeled by  
110 MEGANv2.1 were overestimated by approximately 30–60%, whereas anthropogenic  
111 VOC emissions derived from the RETRO inventory were underestimated by 13–16%.  
112 Cao et al. (2018) employed the GEOS-Chem model and its adjoint, incorporating  
113 tropospheric HCHO and CHOCHO column data from the GOME-2A and OMI  
114 satellites as constraints, to quantify Chinese NMVOC emissions. They demonstrated a  
115 low bias in the MEGAN model, in contrast to the significant overestimation shown in  
116 Bauwens et al. (2016), especially in southern China.

117 Several investigations have been conducted to explore the implications of inverted  
118 VOC emissions on surface O<sub>3</sub>. For instance, using the Eulerian box model, Zhou et al.  
119 (2023) employed concurrent VOC measurements to constrain anthropogenic VOC  
120 emissions. This led to improved simulations of VOCs and O<sub>3</sub>, with a reduction in high  
121 emissions by 15%–36% in the Pearl River Delta (PRD) region. Local model biases in  
122 simulating the oxidation of NMVOCs and O<sub>3</sub> are closely related to uncertainties in NO<sub>x</sub>  
123 emissions (Wolfe et al., 2016; Chan Miller et al., 2017). To tackle these critical  
124 questions, Kaiser et al. (2018) applied an adjoint algorithm to estimate isoprene

125 emission over the southeast US by downwardly adjusting anthropogenic  $\text{NO}_x$  emissions  
126 by 50% to rectify  $\text{NO}_2$  simulations. Their findings indicated that isoprene emissions  
127 from MEGAN v2.1 were overestimated by an average of 40%, slightly lower than the  
128 50% reduction in Bauwens et al. (2016). Souri et al. (2020) simultaneously optimized  
129 NMVOC and  $\text{NO}_x$  emissions utilizing OMPS-NM HCHO and OMI  $\text{NO}_2$  retrievals in  
130 East Asia. They found that predominantly anthropogenic NMVOC emissions from  
131 MIX-Asia 2010 increased over the North China Plain (NCP), whereas predominantly  
132 biogenic NMVOC emissions from MEGAN v2.1 decreased over southern China after  
133 the adjustment. Unfortunately, the posterior simulations exacerbated the overestimation  
134 of  $\text{O}_3$  levels in northern China.

135 Most studies regarding the inversion of NMVOC emissions or its impact on  $\text{O}_3$   
136 neglected the uncertainties associated with  $\text{NO}_x$ -dependent production or loss of  
137 NMVOC oxidation and  $\text{O}_3$ . An iteratively nonlinear joint inversion of  $\text{NO}_x$  and  
138 NMVOCs using multi-species observations is expected to minimize the uncertainties  
139 in their emissions and is well-suited to address the intricate relationship among VOC-  
140  $\text{NO}_x$ - $\text{O}_3$ . In this study, we extended the Regional multi-Air Pollutant Assimilation  
141 System (RAPAS) upon the ensemble Kalman filter (EnKF) assimilation algorithm to  
142 enhance the optimization of NMVOC emissions over China, utilizing the  
143 TROPOspheric Monitoring Instrument (TROPOMI) HCHO retrievals with high spatial  
144 coverage and resolution. To more accurately quantify the impact of NMVOC emissions  
145 on  $\text{O}_3$ ,  $\text{NO}_x$  emissions were simultaneously adjusted using nationwide in-situ  $\text{NO}_2$   
146 observations. Process analysis was subsequently employed to quantify various  
147 chemical pathways associated with  $\text{O}_3$  formation and loss. Through a top-down  
148 constraint on both emissions, this study aims to offer a more scientific insight into the  
149 consequences of optimizing NMVOC emissions on  $\text{O}_3$  and contribute to the  
150 development of appropriate emission reduction policies.

## 151 **2 Data and Methods**

### 152 **2.1 Data Assimilation System**

153 The RAPAS system (Feng et al., 2023) has been developed based on a regional  
154 chemical transport model (CTM) and ensemble square root filter (EnSRF) assimilation  
155 modules (Whitaker and Hamill, 2002), which are employed for simulating atmospheric  
156 compositions and inferring anthropogenic emissions by assimilating surface

157 observations, respectively (Feng et al., 2022; Feng et al., 2020). The inversion process  
158 follows a two-step procedure within each inversion window, in which the emissions are  
159 inferred first and then input into the CMAQ model to simulate initial conditions of the  
160 next window. Meanwhile, the optimized emissions are transferred to the next window  
161 as prior emissions. The two-step inversion strategy facilitates error propagation and  
162 iterative emission optimization, which have proven the superiority and robustness of  
163 our system in estimating emissions (Feng et al., 2023). In this study, we extended the  
164 data frame to include the assimilation of TROPOMI HCHO retrievals for optimizing  
165 NMVOC emissions. Concise descriptions of the forecast model, data assimilation  
166 approach, and experimental settings follow.

### 167 **2.1.1 Atmospheric Transport Model**

168 The Weather Research and Forecast (WRF v4.0) model (Skamarock and Klemp, 2008)  
169 and the Community Multiscale Air Quality Modeling System (CMAQ v5.0.2) (Byun  
170 and Schere, 2006) were applied to simulate meteorological conditions and atmospheric  
171 chemistry, respectively. WRF simulations were conducted with a 27-km horizontal  
172 resolution, covering the entire mainland China on a grid of  $225 \times 165$  cells (Figure 1).  
173 The CMAQ model was run over the same domain, but with a removal of three grid cells  
174 on each side of the WRF domain. The vertical settings in WRF and CMAQ was the  
175 same as Feng et al. (2020). To account for the rapid expansion of urbanization, we  
176 updated underlying surface information for urban and built-up land using the MODIS  
177 Land Cover Type Product (MCD12C1) Version 6.1 of 2022. Chemical lateral boundary  
178 conditions for NO, NO<sub>2</sub>, HCHO, and O<sub>3</sub> were extracted from the output of the global  
179 CTM (i.e., the Whole Atmosphere Community Climate Model, WACCM) with a  
180 resolution of  $0.9^\circ \times 1.25^\circ$  at 6-hour intervals (Marsh et al., 2013). Meanwhile, boundary  
181 conditions for the other NMVOCs were obtained directly from background profiles. In  
182 the first data assimilation (DA) window, chemical initial conditions (excluding  
183 NMVOCs) were also derived from the WACCM outputs, whereas in subsequent  
184 windows, they were derived through forward simulation using optimized emissions  
185 from the previous window. Table S1 lists the detailed physical and chemical  
186 configurations. To assess the impact of updated NMVOC emissions on O<sub>3</sub> production  
187 efficiency, we further decoupled the contribution of the primary chemical processes to  
188 the O<sub>3</sub> levels using the CMAQ Integrated Reaction Rate (IRR) analysis.

190 **2.1.2 EnKF Assimilation Algorithm**

191 The emissions are constrained using the Ensemble Square Root Filter (EnSRF)  
192 algorithm introduced by Whitaker and Hamill (2002). This approach fully accounts for  
193 temporal and geographical variations in both the transportation and chemical reactions  
194 within the emission estimates. During the forecast step, the background ensembles are  
195 derived by applying perturbation to the prior emissions. The perturbed samples are  
196 typically drawn from Gaussian distributions with a mean of zero and a standard  
197 deviation equal to the prior emission uncertainty in each grid cell. Ensemble runs of the  
198 CMAQ model were subsequently performed to propagate the background errors with  
199 each ensemble sample of state vectors.

200 In the analysis step, the ensemble mean  $\bar{\mathbf{X}}^a$  of the analyzed state is regarded as the best  
201 estimate of emissions, which is obtained by updating the background ensemble mean  
202 through the following equations:

203 
$$\bar{\mathbf{X}}^a = \bar{\mathbf{X}}^b + \mathbf{K}(\mathbf{y} - \mathbf{H}\bar{\mathbf{X}}^b) \quad (1)$$

204 
$$\mathbf{K} = \mathbf{P}^b \mathbf{H}^T (\mathbf{H} \mathbf{P}^b \mathbf{H}^T + \mathbf{R})^{-1} \quad (2)$$

205 where  $\mathbf{y}$  is the observational vector;  $\mathbf{H}$  represents the observation operator mapping  
206 model space to observation space; The expression  $\mathbf{y} - \mathbf{H}\bar{\mathbf{X}}^b$  quantifies the disparities  
207 between simulated and observed concentrations;  $\mathbf{P}^b \mathbf{H}^T$  illustrates how uncertainties in  
208 emissions relate to uncertainties in simulated concentrations; The Kalman gain matrix  
209  $\mathbf{K}$ , dependent on background error covariance  $\mathbf{P}^b$  and observation error covariance  $\mathbf{R}$ ,  
210 determines the relative contributions to the updated analysis.

211 State variables for emissions include  $\text{NO}_x$  and NMVOCs. To reduce the degree of  
212 freedom in the analysis and avoid the difficulty associated with estimating spatio-  
213 temporal variations in background errors for individual species, we focus on optimizing  
214 the lumped total NMVOC emissions. During the forecast step, we differentiate  
215 individual NMVOC species emissions from the total NMVOC emissions using bottom-  
216 up statistical information. For a consistent comparison between simulations and  
217 observations, model-simulated  $\text{NO}_2$  were diagnosed at the time and location of surface  
218  $\text{NO}_2$  measurements, whereas model-simulated HCHO was horizontally sampled to  
219 align with TROPOMI HCHO VCD retrievals, and subsequently integrated vertically.

220 In this study, the DA window was set to one day and daily TROPOMI HCHO columns  
221 were utilized as observational constraints in our inversion framework. The ensemble  
222 size was set to 50 to strike a balance between computational cost and inversion accuracy.  
223 To reduce the impact of unrealistic long-distance error correlations, the Gaspari and  
224 Cohn function (Gaspari and Cohn, 1999) was utilized as covariance localization to  
225 ensure the meaningful influence of observations on state variables within a specified  
226 cutoff radius, while mitigating their negative impacts on distant state variables. The  
227 optimal localization scale is interconnected with factors such as the assimilation  
228 window, the dynamic system, and the lifetime of chemical species. Given the average  
229 wind speed of 2.8 m/s (Table S2) and a DA window of 1 day, the localization scales for  
230 NO<sub>2</sub> and HCHO, both characterized as highly reactive species with lifespans of just a  
231 few hours, were set to 150 km and 100 km, respectively.

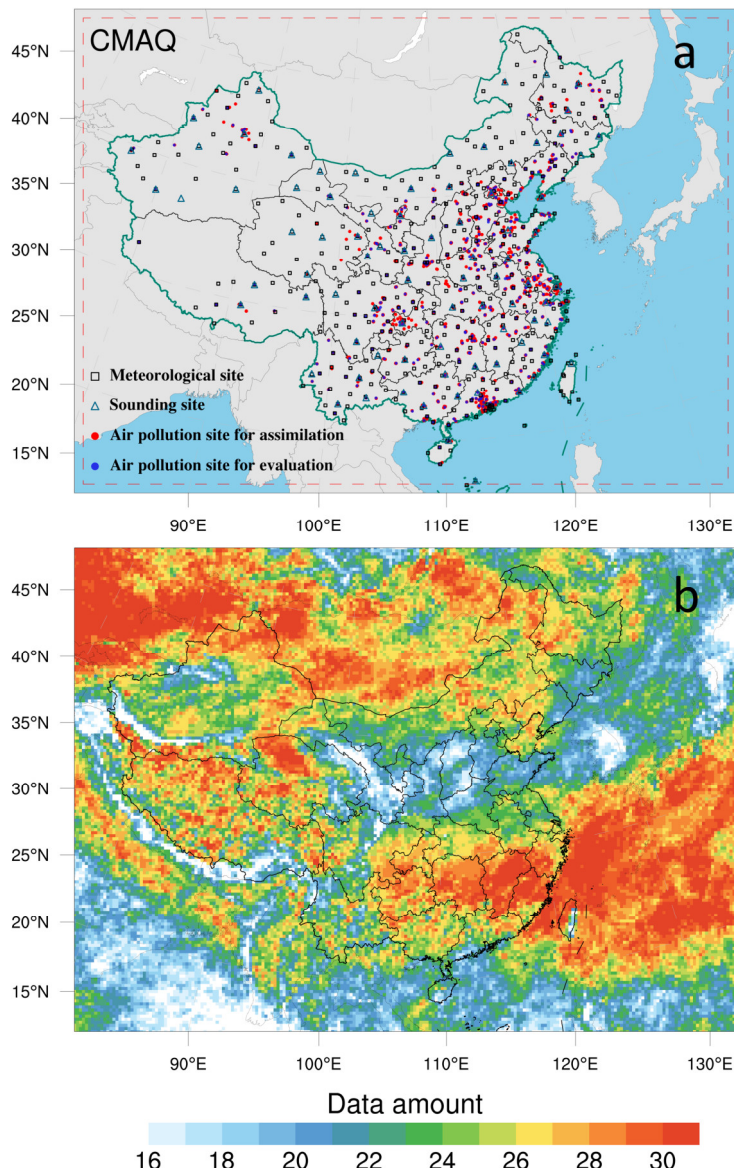
## 232 **2.2 Observation Data and Errors**

233 Considering the availability of HCHO data, we utilized daily offline retrievals of  
234 tropospheric HCHO columns from Sentinel-5P (S5P) L3 TROPOMI data obtained  
235 through Google Earth Engine (De Smedt et al., 2018). The S5P satellite follows a near-  
236 polar sun-synchronous orbit at an altitude of 824 km with a 17-day repeating cycle. It  
237 crosses the Equator at 13:30 local solar time (LST) on the ascending node. The spatial  
238 resolution at nadir was refined to  $3.5 \times 5.5 \text{ km}^2$  on 6 August 2019. Following the  
239 recommendations in the S5P HCHO product user manual, we filtered the source data  
240 to exclude pixels with qa\_value less than 0.5 for HCHO column number density and  
241 0.8 for aerosol index (AER\_AI). The remaining high-quality pixels with minimal  
242 snow/ice or cloud interference are averaged to 27-km grids. Figure 1b illustrates the  
243 coverage and data amount of TROPOMI HCHO retrievals in August 2022 after  
244 processing. Although the distribution of filtered data exhibits spatial non-uniformity,  
245 most grid cells have observational coverage for over half of the time, particularly in the  
246 southern region of China where NMVOC emissions are higher. Based on validation  
247 against a global network of 25 ground-based Fourier transform infrared (FTIR) column  
248 measurements (Vigouroux et al., 2020), TROPOMI HCHO overestimates by 25%  
249 ( $<2.5 \times 10^{15} \text{ molec cm}^{-2}$ ) in clean regions and underestimates by 30% ( $>8 \times 10^{15} \text{ molec}$   
250  $\text{cm}^{-2}$ ) in polluted regions. Therefore, we set the measurement error to 30%. To evaluate  
251 the effect of observational data retrieval errors on emission estimates, we conducted a  
252 sensitivity experiment in which HCHO columns were empirically bias-corrected

253 according to the error characteristics described above (Figure S1). The posterior  
254 emissions increased by 12.8% compared to those in the base experiment (EMDA),  
255 indicating that the existing retrieval error in HCHO measurements likely exerts an  
256 influence on the estimation of NMVOC emissions. The representation error can be  
257 disregarded because the model's resolution significantly surpasses that of the  
258 TROPOMI pixels.

259 To address the chemical feedback among VOC-NO<sub>x</sub>-O<sub>3</sub>, we also simultaneously  
260 optimized NO<sub>x</sub> emissions by assimilating in-situ NO<sub>2</sub> observations. The extensively  
261 covered and high-precision monitoring network can provide sufficient constraints for  
262 emission inversion (Figure 1a). Hourly averaged surface NO<sub>2</sub> observations from  
263 national control air quality stations obtained from the Ministry of Ecology and  
264 Environment of the People's Republic of China (<http://106.37.208.228:8082/>, last  
265 access: 5 May 2023). In case where multiple stations are located within the same grid,  
266 a random site is chosen for validation, while the remaining sites are averaged to mitigate  
267 the impact of error correlation (Houtekamer and Zhang, 2016) for assimilation. In total,  
268 1276 stations were chosen for assimilation and an additional 425 independent stations  
269 were selected for verification (Figure 1a). The observation error covariance matrix **R**  
270 incorporates contributions from both measurement and representation errors. The  
271 measurement error is defined as  $\varepsilon_0 = 1.0 + 0.005 \times \Pi_0$ , where  $\Pi_0$  represents the  
272 observed NO<sub>2</sub> concentration. Following the approach of Elbern et al. (2007) and Feng  
273 et al. (2018), the representative error is defined as  $\varepsilon_r = \gamma \varepsilon_0 \sqrt{\Delta l / L}$ , where  $\gamma$  is a tunable  
274 parameter (here,  $\gamma=0.5$ ),  $\Delta l$  is the grid spacing (27 km), and  $L$  is the radius (here,  $L=0.5$ )  
275 of the observation's influence area. The total observation error ( $r$ ) was defined as  $r =$   
276  $\sqrt{\varepsilon_0^2 + \varepsilon_r^2}$ . The observation errors are assumed to be uncorrelated so that **R** is a  
277 diagonal matrix.

278



279

280 **Figure 1.** Model domain and observation network (a) and data amount of TROPOMI  
 281 HCHO retrievals during August 2022 in each grid (b). The red dashed frame delineates  
 282 the CMAQ computational domain; black squares denote surface meteorological  
 283 measurement sites; navy triangles indicate sounding sites (Text S1), and red and blue  
 284 dots represent air pollution measurement sites, where red dots are used for assimilation  
 285 and blue dots for independent evaluation.

### 286 2.3 Prior Emissions and Uncertainties

287 The prior anthropogenic  $\text{NO}_x$  and NMVOC emissions for China were obtained from  
 288 the most recent Multi-resolution Emission Inventory for China of 2020 (MEIC,  
 289 <http://www.meicmodel.org/>, last access: 8 May 2023) (Zhang et al., 2009). For  
 290 anthropogenic emissions outside China, we utilized the mosaic Asian anthropogenic

291 emission inventory (MIX) for the base year of 2010 (Li et al., 2017b). The daily  
292 emission inventory, which was arithmetically averaged from the combined monthly  
293 emission inventory, was employed as the first guess. Ship emissions were derived from  
294 the shipping emission inventory model (SEIM) for 2017, which was calculated based  
295 on the observed vessel automatic identification system (Liu et al., 2017). Biomass  
296 burning emissions were retrieved from the Global Fire Emissions Database version 4.1  
297 (GFEDv4, <https://www.globalfiredata.org/>, last access: 8 May 2023) (van der Werf et  
298 al., 2017; Mu et al., 2011). Biogenic NO<sub>x</sub> and NMVOC emissions were calculated using  
299 the Model of Emissions of Gases and Aerosols from Nature (MEGAN) developed by  
300 Guenther et al. (2012).

301 As previously mentioned, the optimized emissions are transferred to the next DA  
302 window as prior emissions for iterative inversion. For biogenic emissions, it is  
303 decomposed into hourly scales based on the daily varying temporal profiles in MEGAN  
304 as model inputs. Daily emission variations will largely dominate the uncertainty in  
305 emissions. Taking into account compensating for model errors and avoiding filter  
306 divergence, we consistently applied an uncertainty of 25% to each model grid of NO<sub>x</sub>  
307 emissions at each DA window, as in Feng et al. (2020). NMVOC emissions typically  
308 exhibit greater uncertainties compared to NO<sub>x</sub> emissions (Li et al., 2017b). Based on  
309 model evaluation, the uncertainty of NMVOC emissions was set to 40% (Kaiser et al.,  
310 2018; Souri et al., 2020; Cao et al., 2018). A sensitivity experiment involving a doubling  
311 of the prior uncertainty (80%) revealed that the differences in posterior NMVOC  
312 emissions amounted to a mere 0.2% (Figure S2). The implementation of a ‘two-step’  
313 inversion strategy allows for the timely correction of residual errors from the previous  
314 assimilation window in the current window, thus ensuring that the RAPAS system has  
315 a relatively low dependence on prior uncertainty settings. This study also addresses  
316 uncertainties in emissions for CO, SO<sub>2</sub>, primary PM<sub>2.5</sub>, and coarse PM<sub>10</sub> to consider the  
317 chemical feedback between different species following Feng et al. (2023).

### 318 **3 Experimental Design**

319 During the summer of 2022, southern China experienced severe heatwave conditions.  
320 The combination of high temperatures and drought had a pronounced effect on  
321 vegetation growth and NMVOC emissions, thereby influencing O<sub>3</sub> production (Wang  
322 et al., 2023). Consequently, we opted to focus on August 2022, as it presented an ideal  
323 period for testing the capabilities of our DA system. Before implementing the emission

324 inversion, a relatively perfect initial field is generated at 0000 UTC on August 1 2022  
 325 through conducting a 5-day simulation with 6-hour interval 3D-Var data assimilation.  
 326 Subsequently, daily emissions are continuously updated over the entire month of  
 327 August (EMDA). Additionally, we designed a sensitivity experiment (EMS) to illustrate  
 328 the significance of optimizing  $\text{NO}_x$  emissions in quantifying VOC- $\text{O}_3$  chemical  
 329 reactions. In this experiment,  $\text{NO}_x$  emissions were not optimized. To validate the  
 330 posterior emissions of  $\text{NO}_x$  and NMVOCs in EMDA, we compared two parallel  
 331 forward simulation experiments, denoted as CEP and VEP, corresponding to prior and  
 332 posterior emission scenarios, respectively, against  $\text{NO}_2$  and HCHO measurements. To  
 333 investigate the impact of optimizing NMVOC emissions on the secondary production  
 334 and loss of surface  $\text{O}_3$ , a forward simulation experiment (CEP1) was conducted with  
 335 the prior NMVOC emissions and the posterior  $\text{NO}_x$  emissions. Another forward  
 336 modelling experiment (CEP2) used the posterior emissions of EMS to evaluate its  
 337 performance. All experiments employ identical meteorological fields, as well as the  
 338 same gas-phase and aerosol modules. Table 1 summarizes the different emission  
 339 inversion and validation experiments conducted in this study.

340 **Table 1.** The assimilation, sensitivity, and validation experiments conducted in this  
 341 study.

Exp. Type	Exp. Name	NMVOC emissions	$\text{NO}_x$ emissions
Assimilation	EMDA	MEIC 2020 and MEGAN for August (the first DA window), optimized emissions of the previous window (other DA windows)	MEIC 2020 and MEGAN for August (the first DA window), optimized emissions of the previous window (other DA windows)
Sensitivity	EMS	Same as EMDA	MEIC 2020 and MEGAN for August
	CEP	MEIC 2020 and MEGAN for August	MEIC 2020 and MEGAN for August
	VEP	Posterior emissions of EMDA	Posterior emissions of EMDA
Validation	CEP1	Same as CEP	Posterior emissions of EMDA
	CEP2	Posterior emissions of EMS	Same as CEP

342

343

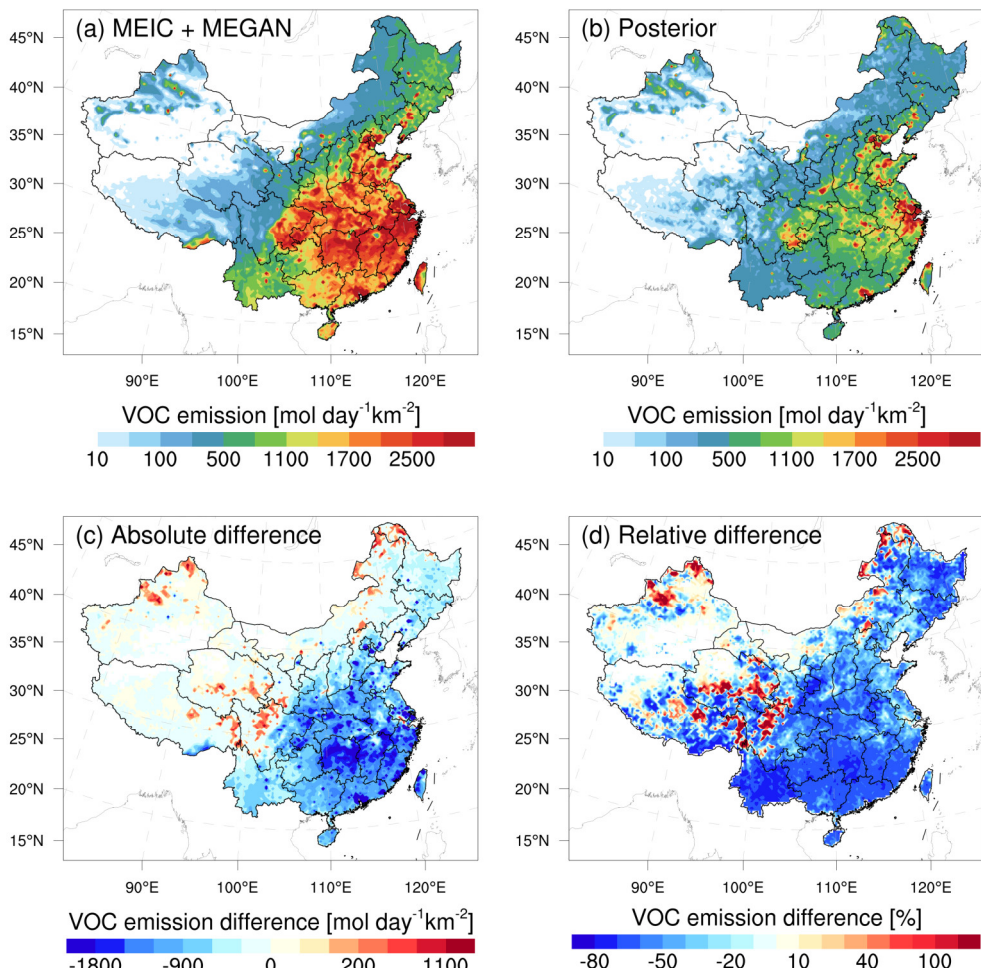
344 **4 Results**

345 **4.1 Inverted Emissions**

346 Figure 2 shows the spatial distribution of temporally averaged prior and posterior  
347 NMVOC emissions, along with their differences, in NMVOC emissions. Hotspots of  
348 prior NMVOC emissions were prevalent across much of central and southern China.  
349 However, posterior NMVOC emissions were predominantly concentrated in the NCP,  
350 Yangtze River Delta (YRD), PRD, and Sichuan Basin (SCB), characterized by high  
351 levels of anthropogenic activity. High emissions are also located in parts of central and  
352 southern China with warm climate favorable for emitting biogenic NMVOCs.  
353 Employing TROPOMI HCHO observations as constraints led to widespread decreases  
354 of approximately 60–70% over these areas, indicating a large substantial of biogenic  
355 NMVOC emissions. In northwestern China, there was a moderate increase in NMVOC  
356 emissions.

357 A potential significant TROPOMI retrieval errors in polluted regions could exacerbate  
358 the emission decreases (Text S2). Additionally, uncertainties in MEGAN  
359 parameterization have significant implications for NMVOC emission estimations,  
360 particularly concerning the responses of vegetation in MEGAN to temperature and  
361 drought stress (Angot et al., 2020; Jiang et al., 2018). Zhang et al. (2021) highlighted  
362 that the temperature-dependent activity factor noticeably increases with rising  
363 temperatures in MEGAN. Wang et al. (2021b) pointed out that the missing of a drought  
364 scheme is one of the factors causing the overestimation of isoprene emissions in  
365 MEGAN. Opacka et al. (2022) optimized the empirical parameter in the MEGANv2.1  
366 soil moisture stress algorithm, resulting in significant reductions in isoprene emissions  
367 and providing better agreement between modelled and observed HCHO temporal  
368 variability in the central U.S. During the study period, China experienced severe  
369 heatwave conditions, which may further hinder the MEGAN's ability to effectively  
370 capture the impacts of high temperatures and drought on vegetation, thus resulting in  
371 significant overestimation in NMVOC emissions (Wang et al., 2022). Ultimately, the  
372 biogenic NMVOC emissions decreased by 53.7%, which was higher than the 43.4%  
373 decrease in anthropogenic NMVOC emissions (Figure S3). NeverthelessOverall,  
374 the large magnitude of emission reductionsdecrease of 50.2% in our inversion is  
375 comparable to studies in southern China (Bauwens et al., 2016; Zhou et al., 2023),  
376 southeastern US (Kaiser et al., 2018), Africa (Marais et al., 2014), India (Chaliyakunnel

377 et al., 2019), Amazonia (Bauwens et al., 2016), and parts of Europe (Curci et al., 2010),  
 378 but opposite to the large-scale emission increase over China in Cao et al. (2018). For  
 379 NO<sub>x</sub> (Figure S43), the nationwide total emissions decreased by 10.2%, with the main  
 380 reductions concentrated in the NCP, YRD, parts of Central China, and most key urban  
 381 areas.



382 **Figure 2.** Spatial distribution of the time-averaged (a) prior emissions (MEIC 2020 +  
 383 MEGAN), (b) posterior emissions, (c) absolute difference (posterior minus prior), and  
 384 (d) relative difference of NMVOCs over China.

386 Table 2 shows the changes in emissions of biogenic NMVOCs across different land  
 387 cover types (Figure S54) after inversion. The most significant reduction in biogenic  
 388 emissions occurred within woody savannas, accounting for 26.9% of the overall  
 389 reduction, followed by savannas and croplands, accounting for 21.2% and 17.2%  
 390 respectively. Among all vegetation types, the broadleaf evergreen forests, recognized  
 391 as the primary source of isoprene emission (Wang et al., 2021a), presented the greatest  
 392 uncertainty, with NMVOC emissions experiencing a significant reduction of 66.2%.

393 Standard emission rates in MEGAN are derived from leaf- or canopy-scale flux  
394 measurements and extrapolated globally across regions sharing similar landcover  
395 characteristics, based on very limited observations (Guenther et al., 1995). This  
396 methodology introduces biases due to the large variability in emission rates among  
397 plant species.

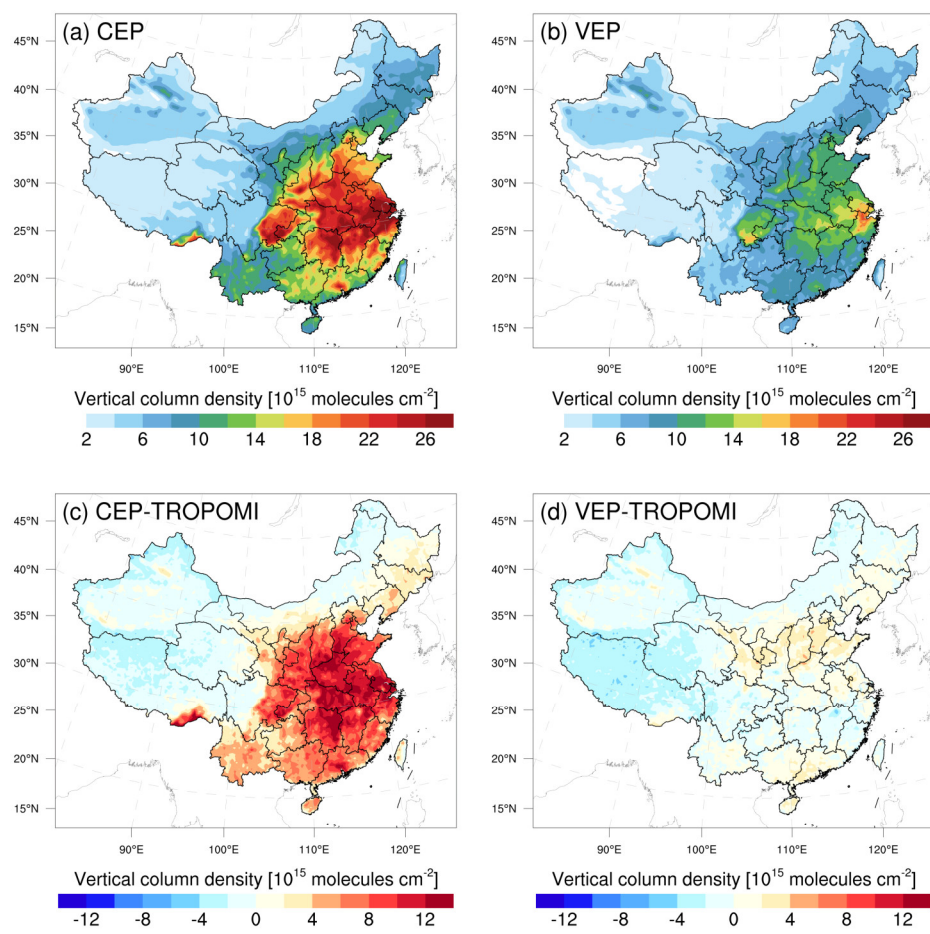
398 **Table 2.** Prior and posterior biogenic NMVOC emissions, as well as their differences  
399 for different land cover types.

Land cover type	Prior	Posterior	Difference
	Mmol/month	Mmol/month	Mmol/month (%)
Evergreen needleleaf forests	955.7	549.3	-406.4 (-42.5)
Evergreen broadleaf forests	13985.1	4728.2	-9256.8 (-66.2)
Deciduous needleleaf forests	46.6	48.8	2.2 (4.7)
Deciduous broadleaf forests	8335.5	3487.4	-4848.1 (-58.2)
Mixed forests	8731.0	3961.7	-4769.4 (-54.6)
Closed shrublands	9.7	3.7	-6.0 (-61.5)
Open shrublands	21.3	8.6	-12.8 (-59.8)
Woody savannas	39327.2	16925.2	-22402.0 (-57.0)
Savannas	28319.7	10629.4	-17690.3 (-62.5)
Grasslands	16912.7	14269.6	-2643.1 (-15.6)
Permanent wetlands	286.1	115.4	-170.8 (-59.7)
Croplands	25537.8	11215.5	-14322.2 (-56.1)
Cropland-natural vegetation mosaics	10894.7	4289.8	-6605.0 (-60.6)
Sparsely vegetated	1814.7	1644.0	-170.6 (-9.4)

400 **4.2 Evaluations for Posterior Emissions**

401 The NO<sub>x</sub> emissions were first evaluated by indirectly comparing the forward simulated  
402 NO<sub>2</sub> concentrations with measurements. As shown in Figure S<sub>65</sub>, the CEP with prior  
403 emissions exhibited positive biases in eastern China and negative biases in western  
404 China. However, when posterior emissions were used in the VEP, a substantial  
405 improvement in simulation performance was observed. Biases were limited to within  
406  $\pm 3 \mu\text{g m}^{-3}$ , and correlation coefficients exceeded 0.7 across the entire region. Figure 3

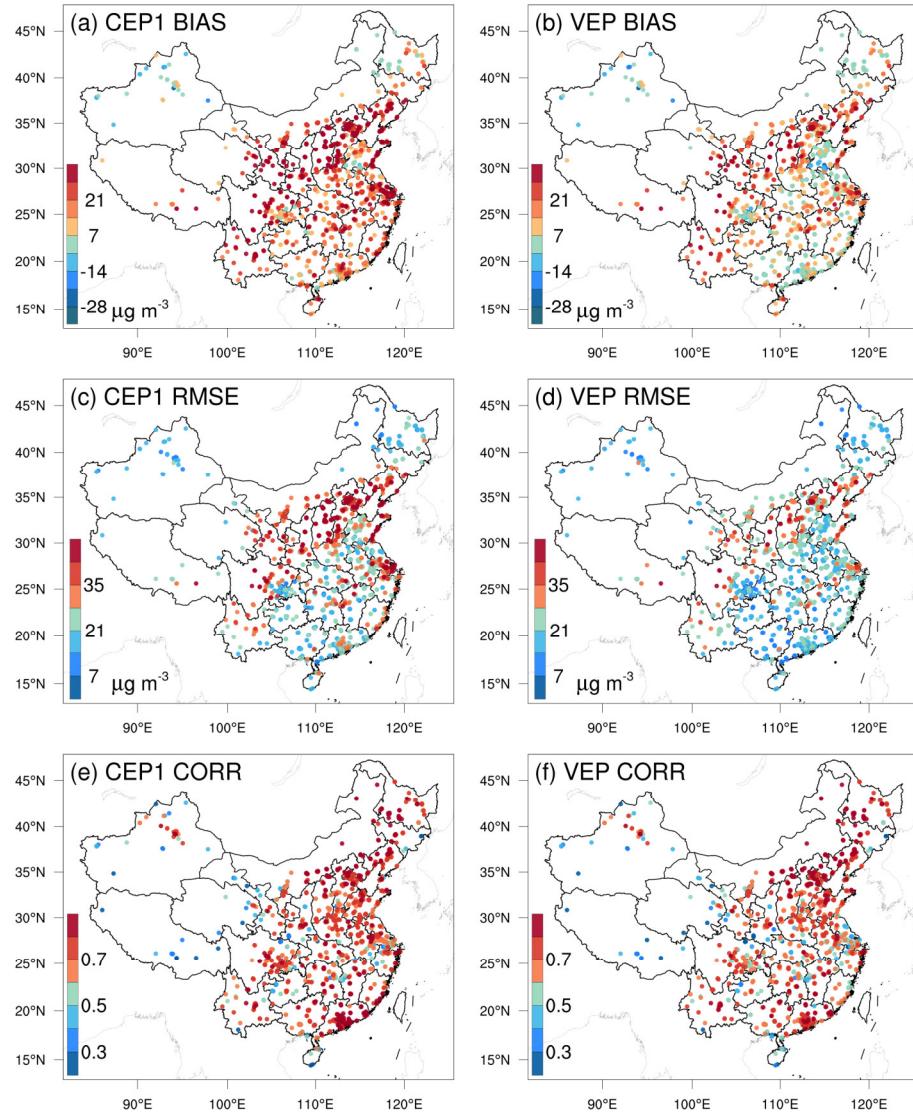
407 presents the simulated HCHO VCDs using prior and posterior NMVOCs emissions,  
 408 along with their associated biases. Both experiments showed high VCDs over central  
 409 and eastern China, especially in the YRD and SCB. However, the CEP displayed  
 410 substantial overestimation across most of mainland China, with the largest bias  
 411 reaching  $12 \times 10^{15}$  molec  $\text{cm}^{-2}$  in Central China. Conversely, the VEP demonstrated  
 412 notable improvements in both the magnitude and spatial distribution of simulated  
 413 HCHO columns after the inversion compared to TROPOMI retrievals. More than 84%  
 414 of the areas exhibited biases of less than  $1 \times 10^{15}$  molec  $\text{cm}^{-2}$ , and no significant spatial  
 415 variation was observed. Overall, the biases in simulated HCHO VCDs decreased by  
 416 75.7% after the inversion. These results emphasize the efficiency of our system in  
 417 reducing uncertainty in both  $\text{NO}_x$  and NMVOC emissions.



418  
 419 **Figure 3.** Simulated HCHO vertical column densities using prior (a) and posterior (b)  
 420 NMVOC emissions, along with their biases (c and d) against TROPOMI measurement.  
 421 All model results were sampled at TROPOMI overpass time.  
 422

423 **4.3 Implications for Surface O<sub>3</sub>**

424 Figure 4 shows the spatial distribution of the mean bias (BIAS), root mean square error  
425 (RMSE), and correlation coefficient (CORR) for simulated O<sub>3</sub> concentrations in the  
426 CEP1 and VEP experiments compared to assimilated observations. Beyond the  
427 northwestern region of China, the CEP1 exhibited significant overestimation  
428 throughout the entire area, with a BIAS of 20.5  $\mu\text{g m}^{-3}$ . In the VEP, the modeled O<sub>3</sub>  
429 chemical production were alleviated, especially in the southern regions of China where  
430 NMVOC emissions had significantly decreased. Overall, observation-constrained  
431 NMVOC emissions resulted in a 49.3% decrease in the BIAS, bringing it down to 10.4  
432  $\mu\text{g m}^{-3}$ . Additionally, the RMSE showed noticeable improvement due to the  
433 assimilation of HCHO observation, reducing the value from 30.9 to 23.3  $\mu\text{g m}^{-3}$ .  
434 Despite a significant reduction in NMVOC emissions after inversion, notable  
435 overestimations persisted in northern provinces such as Liaoning, Hebei, Shanxi, and  
436 Shaanxi. This may be attributed to limited NMVOC constraints resulting from  
437 insufficient observations during the study period (Figures 1b and 3d). The remaining  
438 discrepancies between simulations and observations can be attributed to the combined  
439 results of intricate urban-rural sensitivity regimes and O<sub>3</sub> photochemistry reactions,  
440 which may not be comprehensively represented by CMAQ model, masking any  
441 potential improvement expected from the constrained emissions (See Sect. 4.4). The  
442 CORR was comparable between the CEP1 and VEP experiments, reflecting that the  
443 CMAQ model effectively simulated the temporal variation of O<sub>3</sub> concentrations. The  
444 biases at the independent sites were similar to those at the assimilated sites (Figure S<sup>76</sup>).  
445 In comparison to CEP1, the decreasing ratios in BIAS and RMSE in VEP were 46.7%  
446 and 23.4%, respectively.

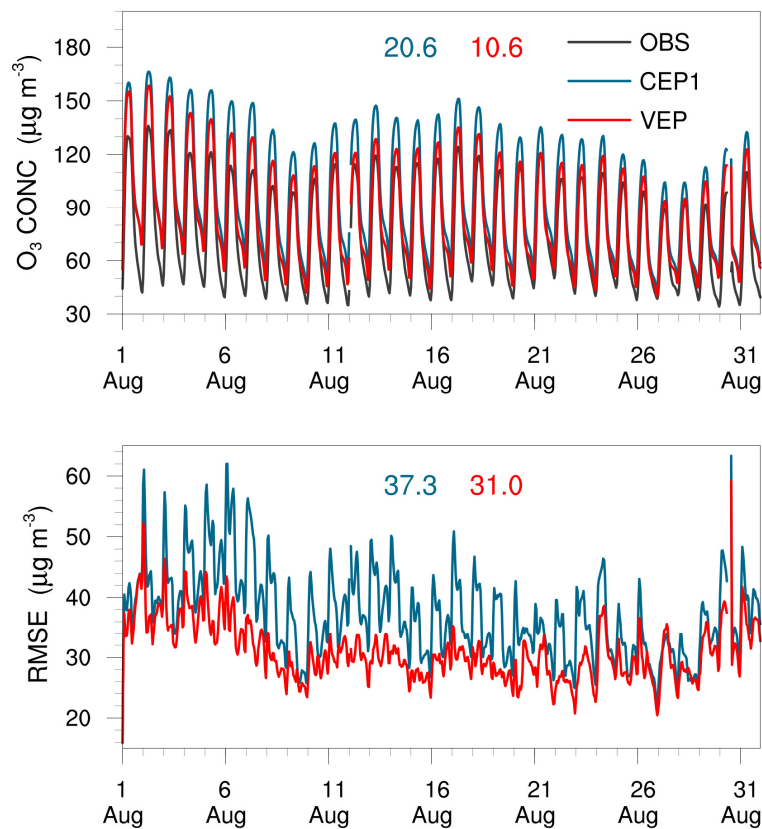


447

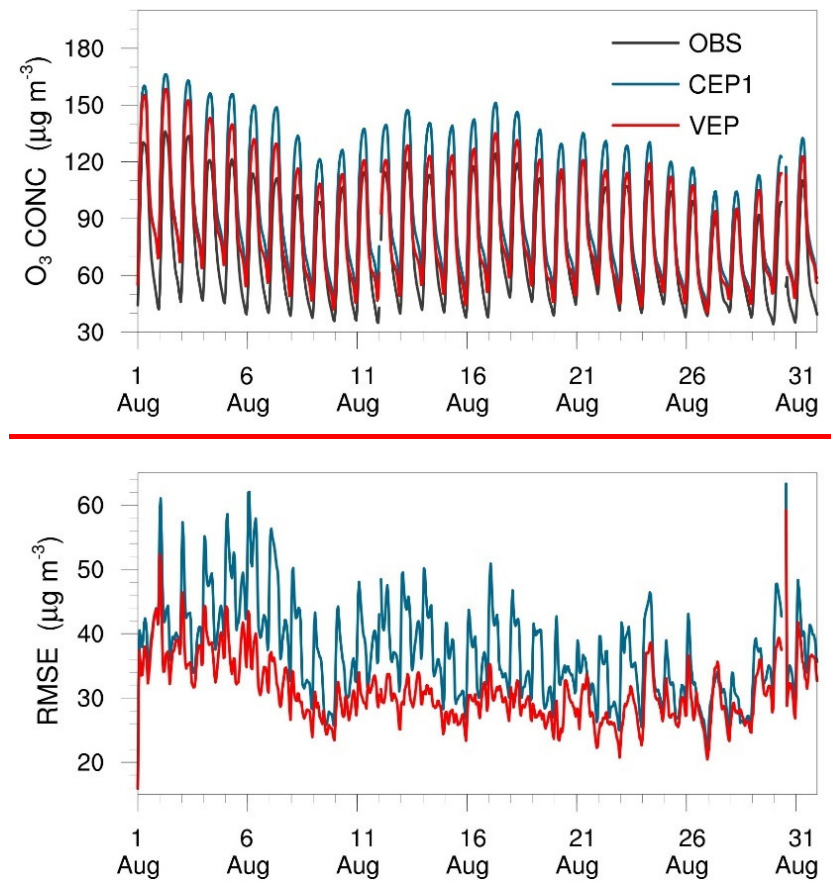
448 **Figure 4.** Spatial distribution of mean bias (BIAS, a and b), root mean square error  
449 (RMSE, c and d), and correlation coefficient (CORR, e and f) for simulated O<sub>3</sub> using  
450 prior (left, CEP1) and posterior (right, VEP) emissions, respectively, against  
451 assimilated observations.

452 Figure 5 shows the time series of simulated and observed hourly O<sub>3</sub> concentrations and  
453 their RMSEs, verified against surface monitoring sites. The VEP achieved better  
454 representations of diurnal O<sub>3</sub> variations compared with those in the CEP1, especially  
455 excelling in reproducing elevated O<sub>3</sub> concentrations at noon. Constraining the NMVOC  
456 emissions also led to better model simulations in terms of RMSE throughout the entire  
457 study period. Time-averaged BIAS and RMSE decreased from 20.6 and 37.3 μg m<sup>-3</sup> to  
458 10.6 and 31.0 μg m<sup>-3</sup>, respectively. We also evaluated the simulation results for seven  
459 key cities (i.e., Beijing, Shanghai, Guangzhou, Wuhan, Chongqing, Yinchuan, and

460 Changchun, which represent key cities in North, East, South, Central, Southwest,  
461 Northwest, and Northeast China, respectively), and the biases in the VEP with posterior  
462 emissions all showed a significant reduction (Figure S8). Overall, the assimilation of  
463 HCHO column observations effectively reduced NMVOC emission uncertainties and  
464 consequently improved simulations of HCHO and O<sub>3</sub>. These improvements hold  
465 promise for further research into the implications of emission optimizations on regional  
466 O<sub>3</sub> photochemistry.



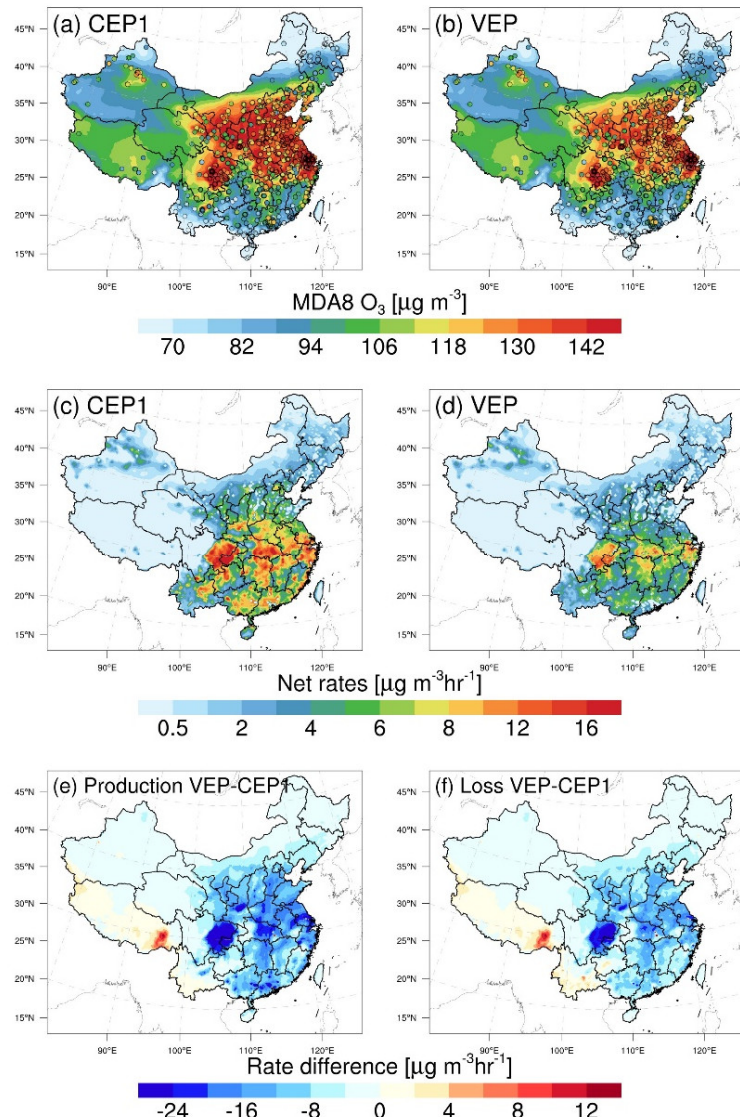
467



468 **Figure 5.** Time series comparison of hourly surface  $O_3$  concentrations ( $\mu\text{g m}^{-3}$ ) and  
 469 RMSE ( $\mu\text{g m}^{-3}$ ) from CEP1 and VEP experiments against all observations-[at 1701](#)  
 470 [monitoring sites. The blue and red values on the graph represent the time-averaged](#)  
 471 [statistics in the CEP1 and VEP experiments, respectively.](#)

472  
 473 As crucial  $O_3$  precursors, the abundance of NMVOCs plays a significant role in  
 474 modulating  $O_3$  production. Here we employed the IRRs to elucidate changes related to  
 475  $O_3$  production and loss at the surface, stemming from constrained  $NO_x$  and NMVOC  
 476 emissions. Figure 6 illustrates comparisons of the simulated maximum daily 8-hour  
 477 average (MDA8) surface  $O_3$  levels and net reaction rates before and after the inversion.  
 478 The CEP1 exhibited an overestimation of  $O_3$  levels, with a BIAS of 22.6% compared  
 479 to observed  $O_3$  concentrations. This overestimation corresponded to the high net  
 480 chemical rates of  $O_3$  in these areas (Figure S97). After inversion,  $O_3$  net rates mitigated  
 481 in most regions. Consequently, the VEP experiment yielded results that closely aligned  
 482 with observations, with a BIAS of 9.2%. Referring to Figure 6e and 6f, differences in  
 483 production rates of  $O_3$  closely track the changes in the NMVOC emissions (Figure 2).  
 484 The discrepancies in specific regions may be attributed to the complex nonlinear  
 485 relationships associated with  $O_3$  and its precursors, which depend on prevailing

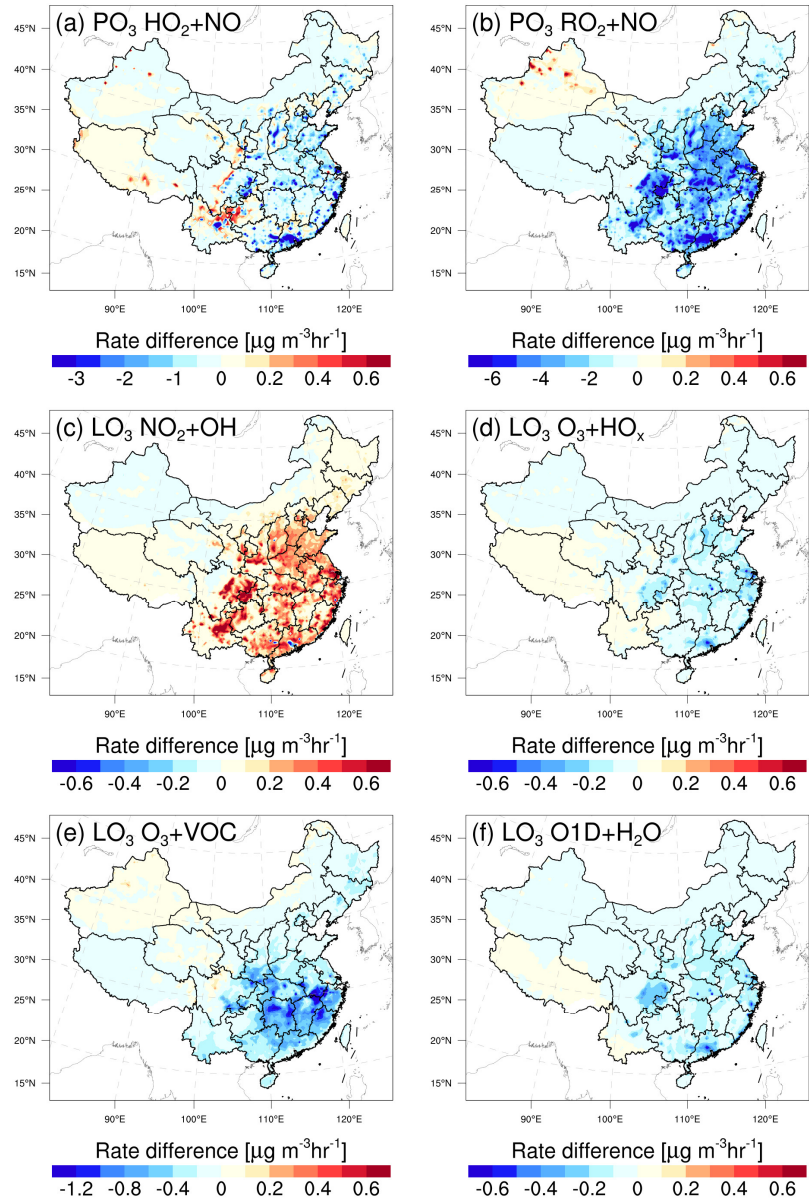
486 chemical regimes and regional transport. Additionally, changes in  $O_3$  production  
487 predominantly drive the overall decrease in  $O_3$  concentrations, outweighing changes in  
488  $O_3$  loss.



489 **Figure 6.** Comparisons of (a, b) simulated maximum daily 8-hour average (MDA8)  $O_3$   
490 concentrations, (c, d) net reaction rates, (e, f) and differences in production and loss  
491 rates between CEP1 and VEP experiments at the surface. Surface MDA8  $O_3$  values  
492 (circles) from the national control air quality stations were overlaid

493 Figure 7 shows the differences in the six principal pathways responsible for  $O_3$  loss and  
494 formation, when comparing simulations employing prior and posterior emissions. The  
495 reactions of  $\text{HO}_2 + \text{NO}$  and  $\text{RO}_2 + \text{NO}$  are treated as the pathways leading to  $O_3$   
496 formation, whereas  $O_3$  loss involves reactions including  $\text{NO}_2 + \text{OH}$ ,  $\text{O}_3 + \text{HO}_2$ ,  $\text{O}_3 +$   
497 NMVOCs, and  $\text{O}_1\text{D} + \text{H}_2\text{O}$  (Wang et al., 2019). Our analysis was focused on the time  
498

499 frame from 12:00 to 18:00 according to China standard time (CST). The differences  
500 were computed by subtracting the simulation with posterior emissions from those with  
501 prior emissions. Following the emission of NMVOCs, they undergo rapid oxidation by  
502 atmospheric hydroxyl (OH) radicals. Due to the substantial decrease in NMVOC  
503 emissions, there was a reduction in the production of hydroperoxy radicals ( $\text{HO}_2$ ) and  
504 organic peroxy radicals ( $\text{RO}_2$ ) (Figure S108). Consequently, this reduction in  $\text{HO}_2/\text{RO}_2$   
505 levels, coupled with their reaction with NO, resulted in diminished  $\text{O}_3$  production  
506 (Figures 7a and 7b). A strong correlation was observed between changes in  $\text{O}_3$   
507 production via the  $\text{RO}_2 + \text{NO}$  reaction and NMVOC emissions (Figure 2), consistent  
508 with the findings of Souri et al. (2020). Typically, in NMVOC-rich environments, a  
509 decrease in NMVOC emissions boosts OH concentrations. Consequently, we noted an  
510 enhancement in the  $\text{NO}_2 + \text{OH}$  reaction in the eastern and central regions of China. In  
511 response to heightened  $\text{HO}_x$  concentrations over these areas, an increased  $\text{O}_3$  loss  
512 through the  $\text{O}_3 + \text{HO}_x$  pathway was observed. Furthermore, we detected a substantial  
513 decrease in  $\text{O}_3$  loss through reactions with NMVOCs, especially in the southern China,  
514 where substantial isoprene emissions are prevalent. This reduction was primarily  
515 attributable to the decrease in NMVOC and  $\text{O}_3$  levels. While the NMVOC +  $\text{O}_3$  reaction  
516 proceeds at a substantially slower rate NMVOC + OH, this specific chemical pathway  
517 remains significant in oxidizing NMVOC and forming  $\text{HO}_x$  in forests areas (Paulson  
518 and Orlando, 1996). The difference in  $\text{O}_3 + \text{H}_2\text{O}$  is primarily driven by the decrease  
519 of  $\text{O}_3$  photolysis. Although the rate of  $\text{O}_3$  loss decreases in some chemical pathways,  
520 overall, the rate of  $\text{O}_3$  production dominates the changes in  $\text{O}_3$  concentration.



521

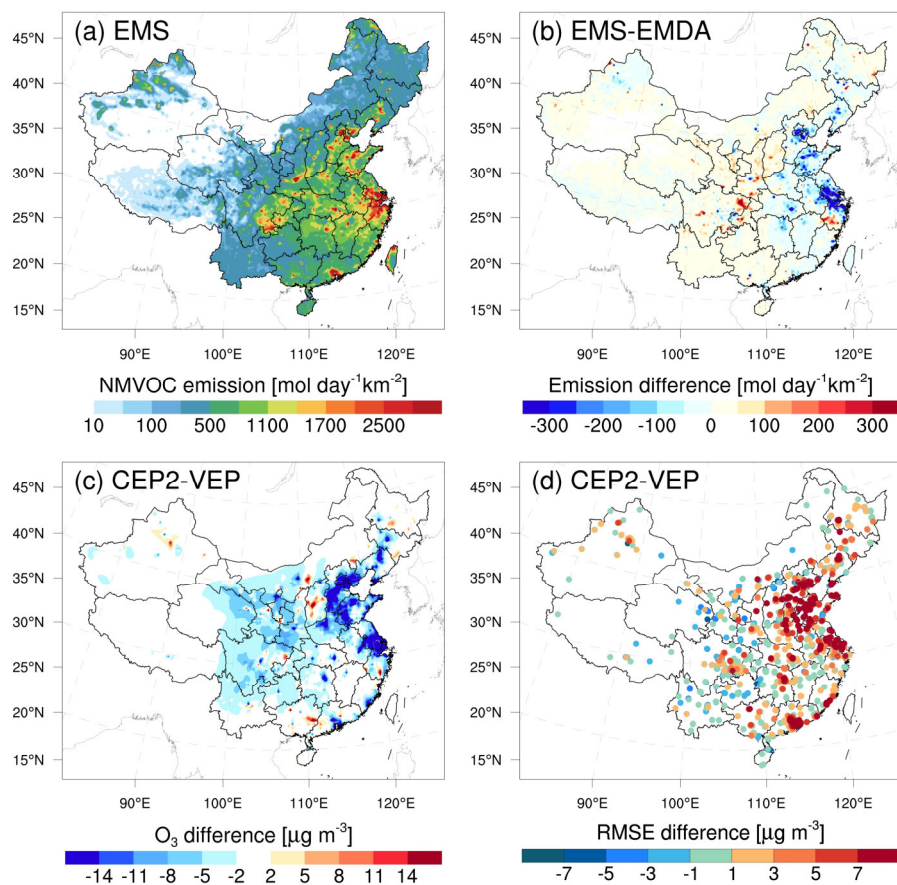
522 **Figure 7.** Differences in six major pathways of O<sub>3</sub> production and loss between CEP1  
 523 and VEP experiments at the surface. Time period: August 2022, 12:00–18:00 CST. PO<sub>3</sub>  
 524 and LO<sub>3</sub> represent the pathways of O<sub>3</sub> formation and loss, respectively.

525 **4.4 Discussions**

526 O<sub>3</sub> simulations over China have a tendency to be overestimated in studies involving  
 527 chemical transport modeling. For example, by intercomparing 14 state-of-the-art CTMs  
 528 with O<sub>3</sub> observations within the framework of the MICS-Asia III, Li et al. (2019)  
 529 identified a substantial overestimation of annual surface O<sub>3</sub> in East Asia, ranging from  
 530 20 to 60  $\mu\text{g m}^{-3}$ . Notably, the NCP exhibited substantial overestimations, with most  
 531 models overestimating O<sub>3</sub> by 100–200% during May–October. Despite our

532 optimization of O<sub>3</sub> precursor emissions, the posterior simulations still exhibit some  
533 degree of overestimation (Figure 4), suggesting that there may indeed be an effect of  
534 systematic bias, such as meteorological fields, spatial resolution, model treatments of  
535 nonlinear photochemistry and other physical processes. The WRF can generally  
536 reproduce meteorological conditions sufficiently in terms of their temporal variation  
537 and magnitude over China (Figure S119), with small biases of -0.5 °C, -5.3%, 0.3 m/s,  
538 and -42.4 m for temperature at 2 m, relative humidity at 2 m, and wind speed at 10 m,  
539 and planetary boundary layer height, respectively. However, due to the relatively coarse  
540 spatial resolution, NO titration effects in urban areas may not be well represented in the  
541 model, which can lead to an overestimation of O<sub>3</sub> in these areas. Additionally, model  
542 inherent errors arising from the model structure, parameterization, and the  
543 simplification or lack of chemical mechanisms inevitably affect the O<sub>3</sub> simulations. For  
544 example, Li et al. (2018) reported that heterogeneous reactions of nitrogen compounds  
545 could weaken the atmospheric oxidation capacity and thus reduce surface O<sub>3</sub>  
546 concentration by 20–40  $\mu\text{g m}^{-3}$  for the polluted regions over China. These reactions  
547 have not been fully incorporated in CMAQ chemical mechanisms. However, there is  
548 still a lack of reasonable and effective algorithms for addressing model errors through  
549 assimilation (Houtekamer and Zhang, 2016). O<sub>3</sub> concentration and NO<sub>x</sub> (VOC)  
550 emissions are positively correlated in the NO<sub>x</sub> (VOC)-limited region and negatively  
551 correlated in the VOC (NO<sub>x</sub>)-limited region (Tang et al., 2011). Therefore, the  
552 uncertainty in NO<sub>x</sub> emissions can affect the model's diagnosis of O<sub>3</sub>-NO<sub>x</sub>-VOC  
553 sensitivity, thereby introducing substantial model errors in the HCHO yield from VOC  
554 oxidation. In the base inversion experiment (EMDA), we simultaneously assimilated  
555 NO<sub>2</sub> and HCHO observations to optimize NO<sub>x</sub> and NMVOC emissions. To evaluate the  
556 impact of optimized NO<sub>x</sub> emissions on O<sub>3</sub>-VOC chemistry, EMS disregarded the  
557 uncertainty of NO<sub>x</sub> and focused on optimizing NMVOC emissions. Compared to the  
558 EMDA, in areas where NO<sub>x</sub> is significantly overestimated, NMVOC emissions in the  
559 EMS have correspondingly decreased (Figure 8b). This might be due to under high-  
560 NO<sub>x</sub> conditions, HCHO production occurs promptly, thereby compensating for the  
561 substantial amount of HCHO already present in the atmosphere by reducing emissions  
562 (Chan Miller et al., 2017). Figure S120 shows comparisons of concentrations and  
563 RMSE between the simulations using posterior emissions from EMS and EMDA  
564 experiments. Compared to VEP, CEP2 showed a larger RMSE, highlighting the  
565 necessity for simultaneous optimization of NO<sub>x</sub> emissions when evaluating the impact

566 of NMVOC emission optimization on  $O_3$ . Additionally, CEP2 using prior  $NO_x$   
 567 emissions exhibited lower  $O_3$  levels over parts of NCP and YRD, as well as some urban  
 568 areas (Figure 8c), but with larger biases and RMSEs (Figure 8d). The reduction in  
 569 NMVOC emissions contributed to a partial decrease in  $O_3$  concentration. More  
 570 significantly, these areas typically align with VOC-limited mechanisms (Wang et al.,  
 571 2019; Wang et al., 2021c). Therefore, the overestimation of  $NO_x$  emissions (Figure S43)  
 572 excessively inhibits  $O_3$  accumulation due to the titration effect, thereby disrupting the  
 573 evaluation of NMVOC contributions to  $O_3$ . This substantial disparity also seriously  
 574 affects  $O_3$  source apportionment, precursor-sensitive area delineation, and emissions  
 575 reduction policy formulation.



577 **Figure 8.** Spatial distribution of (a) posterior emissions in the EMS experiment, (b)  
 578 differences in posterior emissions between EMS and EMDA, and differences in  
 579 simulated (c)  $O_3$  concentrations and (d) RMSE between CEP2 and VEP experiments.  
 580 EMS did not optimize  $NO_x$  emissions compared to EMDA.

581

582 **5 Summary and Conclusions**

583 In this study, we extended the RAPAS assimilation system with the EnKF assimilation  
584 algorithm to optimize NMVOC emissions using the TROPOMI HCHO retrievals.  
585 Taking the MEIC 2020 for anthropogenic emissions and MEGANv2.1 output for  
586 biogenic sources as a priori, NMVOC emissions over China in August 2022 were  
587 inferred. Importantly, we implicitly took the chemical feedback among VOC-NO<sub>x</sub>-O<sub>3</sub>  
588 into account by simultaneously adjusting NO<sub>x</sub> emissions using nationwide in-situ NO<sub>2</sub>  
589 observations. Furthermore, we quantified the impact of NMVOC emission inversion on  
590 surface O<sub>3</sub> pollution using the CMAQ-IRR model.

591 The application of TROPOMI HCHO observations as constraints led to a substantial  
592 reduction of 50.2% compared to the prior emissions for NMVOCs [in August 2022](#). A  
593 domain-wide significant decrease was found over central and southern China with  
594 abundant forests, especially for the broadleaf evergreen forests, implying a considerable  
595 overestimation of biogenic NMVOC emissions. Observation-constrained emissions  
596 significantly improved the performance of surface NO<sub>2</sub> and HCHO column simulations,  
597 reducing biases by 97.4% and 75.7%, respectively. This highlights the effectiveness of  
598 the RAPAS in reducing uncertainty in NO<sub>x</sub> and NMVOC emissions. Isolating the  
599 impact of NO<sub>x</sub> emission changes, the posterior NMVOC emissions significantly  
600 mitigated the overestimation in prior O<sub>3</sub> simulations, resulting in a 49.3% decrease in  
601 surface O<sub>3</sub> biases. This is mainly attributed to a substantial decrease in the RO<sub>2</sub> + NO  
602 reaction rate (a major pathway for O<sub>3</sub> production) and an increase NO<sub>2</sub> + OH reaction  
603 rate (a major pathway for O<sub>3</sub> loss) during the afternoon, resulting in a decrease in the  
604 simulated MDA8 surface O<sub>3</sub> concentrations by approximately 15  $\mu\text{g m}^{-3}$ .

605 Sensitivity inversions demonstrate the robustness of top-down emissions to variations  
606 in prior uncertainty settings, yet they are sensitive to HCHO column biases,  
607 highlighting the importance of comprehensive validation studies utilizing available  
608 remote-sensing data and, if possible, airborne validation campaigns. Moreover, we  
609 found that, in comparison to optimizing NMVOC emissions alone, the joint  
610 optimization of NMVOC and NO<sub>x</sub> emissions can significantly improve the overall  
611 performance of O<sub>3</sub> simulations. Ignoring errors in NO<sub>x</sub> emissions introduces uncertainty  
612 in quantifying the impact of NMVOC emissions on surface O<sub>3</sub>, especially in areas  
613 where overestimated NO<sub>x</sub> emissions can unrealistically amplify titration effects,

614 highlighting the necessity of simultaneous optimization of NO<sub>x</sub> emissions.

615

## 616 **Data availability**

617 The observations used for assimilation and the optimized emissions in this study can be  
618 accessed at <https://doi.org/10.5281/zenodo.10079006> (Feng and Jiang, 2023).

619

## 620 **Author contribution**

621 SF and FJ conceived and designed the research. SF developed the data assimilation  
622 code, analyzed data, and prepared the paper with contributions from all co-authors. FJ  
623 supervised and assisted in conceptualization and writing. TQ, NW, MJ, SZ, JC, FY, and  
624 WJ reviewed and commented on the paper.

625

## 626 **Competing interests**

627 The authors declare that they have no conflict of interest.

628

## 629 **Acknowledgements**

630 This work is supported by the National Key R&D Program of China (Grant No.  
631 2022YFB3904801), the National Natural Science Foundation of China (Grant No:  
632 42305116 and 42377102), the Natural Science Foundation of Jiangsu Province of China  
633 (Grant No: BK20230801), and the Hangzhou Agricultural and Social Development  
634 Scientific Research Project (Grant No: 202203B29). The authors also gratefully  
635 acknowledge the High-Performance Computing Center (HPCC) of Nanjing University  
636 for doing the numerical calculations in this paper on its blade cluster system.

637

## 638 **References**

639 Angot, H., McErlean, K., Hu, L., Millet, D. B., Hueber, J., Cui, K., Moss, J., Wielgasz, C., Milligan,  
640 T., Ketcherside, D., Bret-Harte, M. S., and Helmig, D.: Biogenic volatile organic compound  
641 ambient mixing ratios and emission rates in the Alaskan Arctic tundra, *Biogeosciences*, 17,  
642 6219-6236, 10.5194/bg-17-6219-2020, 2020.

643 Bauwens, M., Stavrakou, T., Müller, J. F., De Smedt, I., Van Roozendael, M., van der Werf, G. R.,  
644 Wiedinmyer, C., Kaiser, J. W., Sindelarova, K., and Guenther, A.: Nine years of global  
645 hydrocarbon emissions based on source inversion of OMI formaldehyde observations, *Atmos.*  
646 *Chem. Phys.*, 16, 10133-10158, 10.5194/acp-16-10133-2016, 2016.

647 Byun, D., and Schere, K. L.: Review of the governing equations, computational algorithms, and  
648 other components of the models-3 Community Multiscale Air Quality (CMAQ) modeling  
649 system, *Applied Mechanics Reviews*, 59, 51-77, 10.1115/1.2128636, 2006.

650 Cao, H., Fu, T. M., Zhang, L., Henze, D. K., Miller, C. C., Lerot, C., Abad, G. G., De Smedt, I.,  
651 Zhang, Q., van Roozendael, M., Hendrick, F., Chance, K., Li, J., Zheng, J., and Zhao, Y.:  
652 Adjoint inversion of Chinese non-methane volatile organic compound emissions using space-  
653 based observations of formaldehyde and glyoxal, *Atmos. Chem. Phys.*, 18, 15017-15046,  
654 10.5194/acp-18-15017-2018, 2018.

655 Chaliyakunnel, S., Millet, D. B., and Chen, X.: Constraining Emissions of Volatile Organic  
656 Compounds Over the Indian Subcontinent Using Space-Based Formaldehyde Measurements,  
657 *Journal of Geophysical Research: Atmospheres*, 124, 10525-10545, 10.1029/2019JD031262,  
658 2019.

659 Chan Miller, C., Jacob, D. J., Marais, E. A., Yu, K., Travis, K. R., Kim, P. S., Fisher, J. A., Zhu, L.,  
660 Wolfe, G. M., Hanisco, T. F., Keutsch, F. N., Kaiser, J., Min, K. E., Brown, S. S., Washenfelder,  
661 R. A., González Abad, G., and Chance, K.: Glyoxal yield from isoprene oxidation and relation  
662 to formaldehyde: chemical mechanism, constraints from SENEX aircraft observations, and  
663 interpretation of OMI satellite data, *Atmos. Chem. Phys.*, 17, 8725-8738, 10.5194/acp-17-  
664 8725-2017, 2017.

665 Cheng, S., Cheng, X., Ma, J., Xu, X., Zhang, W., Lv, J., Bai, G., Chen, B., Ma, S., Ziegler, S., Donner,  
666 S., and Wagner, T.: Mobile MAX-DOAS observations of tropospheric NO<sub>2</sub> and HCHO during  
667 summer over the Three Rivers' Source region in China, *Atmos. Chem. Phys.*, 23, 3655-3677,  
668 10.5194/acp-23-3655-2023, 2023.

669 Curci, G., Palmer, P. I., Kurosu, T. P., Chance, K., and Visconti, G.: Estimating European volatile  
670 organic compound emissions using satellite observations of formaldehyde from the Ozone  
671 Monitoring Instrument, *Atmos. Chem. Phys.*, 10, 11501-11517, 10.5194/acp-10-11501-2010,  
672 2010.

673 De Smedt, I., Theys, N., Yu, H., Danckaert, T., Lerot, C., Compernolle, S., Van Roozendael, M.,  
674 Richter, A., Hilboll, A., Peters, E., Pedernana, M., Loyola, D., Beirle, S., Wagner, T., Eskes,  
675 H., van Geffen, J., Boersma, K. F., and Veefkind, P.: Algorithm theoretical baseline for  
676 formaldehyde retrievals from S5P TROPOMI and from the QA4ECV project, *Atmos. Meas.  
677 Tech.*, 11, 2395-2426, 10.5194/amt-11-2395-2018, 2018.

678 Elbern, H., Strunk, A., Schmidt, H., and Talagrand, O.: Emission rate and chemical state estimation  
679 by 4-dimensional variational inversion, *Atmospheric Chemistry and Physics*, 7, 3749-3769,  
680 10.5194/acp-7-3749-2007, 2007.

681 Fang, X., Shao, M., Stohl, A., Zhang, Q., Zheng, J., Guo, H., Wang, C., Wang, M., Ou, J., Thompson,  
682 R. L., and Prinn, R. G.: Top-down estimates of benzene and toluene emissions in the Pearl  
683 River Delta and Hong Kong, China, *Atmos. Chem. Phys.*, 16, 3369-3382, 10.5194/acp-16-  
684 3369-2016, 2016.

685 Feng, S., Jiang, F., Jiang, Z., Wang, H., Cai, Z., and Zhang, L.: Impact of 3DVAR assimilation of  
686 surface PM2.5 observations on PM2.5 forecasts over China during wintertime, *Atmospheric  
687 Environment*, 187, 34-49, 10.1016/j.atmosenv.2018.05.049, 2018.

688 Feng, S., Jiang, F., Wang, H., Wang, H., Ju, W., Shen, Y., Zheng, Y., Wu, Z., and Ding, A.: NO<sub>x</sub>  
689 Emission Changes Over China During the COVID-19 Epidemic Inferred From Surface NO<sub>2</sub>  
690 Observations, *Geophysical Research Letters*, 47, 10.1029/2020gl090080, 2020.

691 Feng, S., Jiang, F., Wang, H., Shen, Y., Zheng, Y., Zhang, L., Lou, C., and Ju, W.: Anthropogenic  
692 emissions estimated using surface observations and their impacts on PM2.5 source  
693 apportionment over the Yangtze River Delta, China, *Science of The Total Environment*, 828,  
694 154522, 10.1016/j.scitotenv.2022.154522, 2022.

695 Feng, S., Jiang, F., Wu, Z., Wang, H., He, W., Shen, Y., Zhang, L., Zheng, Y., Lou, C., Jiang, Z., and  
696 Ju, W.: A Regional multi-Air Pollutant Assimilation System (RAPAS v1.0) for emission  
697 estimates: system development and application, *Geosci. Model Dev.*, 16, 5949-5977,  
698 10.5194/gmd-16-5949-2023, 2023.

699 Gaspari, G., and Cohn, S. E.: Construction of correlation functions in two and three dimensions,  
700 *Quarterly Journal of the Royal Meteorological Society*, 125, 723-757, 10.1256/smsqj.55416,  
701 1999.

702 Guenther, A. B., Jiang, X., Heald, C. L., Sakulyanontvittaya, T., Duhl, T., Emmons, L. K., and Wang,  
703 X.: The Model of Emissions of Gases and Aerosols from Nature version 2.1 (MEGAN2.1): an  
704 extended and updated framework for modeling biogenic emissions, *Geoscientific Model  
705 Development*, 5, 1471-1492, 10.5194/gmd-5-1471-2012, 2012.

706 Hong, C., Zhang, Q., He, K., Guan, D., Li, M., Liu, F., and Zheng, B.: Variations of China's emission  
707 estimates: response to uncertainties in energy statistics, *Atmos. Chem. Phys.*, 17, 1227-1239,  
708 10.5194/acp-17-1227-2017, 2017.

709 Hong, Q., Liu, C., Hu, Q., Zhang, Y., Xing, C., Su, W., Ji, X., and Xiao, S.: Evaluating the feasibility  
710 of formaldehyde derived from hyperspectral remote sensing as a proxy for volatile organic  
711 compounds, *Atmospheric Research*, 264, 105777, 10.1016/j.atmosres.2021.105777, 2021.

712 Houtekamer, P. L., and Zhang, F.: Review of the Ensemble Kalman Filter for Atmospheric Data  
713 Assimilation, *Monthly Weather Review*, 144, 4489-4532, 10.1175/mwr-d-15-0440.1, 2016.

714 Jiang, X., Guenther, A., Potosnak, M., Geron, C., Seco, R., Karl, T., Kim, S., Gu, L., and Pallardy,  
715 S.: Isoprene emission response to drought and the impact on global atmospheric chemistry,  
716 *Atmospheric Environment*, 183, 69-83, 10.1016/j.atmosenv.2018.01.026, 2018.

717 Kaiser, J., Jacob, D. J., Zhu, L., Travis, K. R., Fisher, J. A., González Abad, G., Zhang, L., Zhang,  
718 X., Fried, A., Crounse, J. D., St. Clair, J. M., and Wisthaler, A.: High-resolution inversion of  
719 OMI formaldehyde columns to quantify isoprene emission on ecosystem-relevant scales:  
720 application to the southeast US, *Atmos. Chem. Phys.*, 18, 5483-5497, 10.5194/acp-18-5483-  
721 2018, 2018.

722 Li, B., Ho, S. S. H., Li, X., Guo, L., Chen, A., Hu, L., Yang, Y., Chen, D., Lin, A., and Fang, X.: A  
723 comprehensive review on anthropogenic volatile organic compounds (VOCs) emission  
724 estimates in China: Comparison and outlook, *Environment International*, 156, 106710,  
725 10.1016/j.envint.2021.106710, 2021.

726 Li, J., Chen, X., Wang, Z., Du, H., Yang, W., Sun, Y., Hu, B., Li, J., Wang, W., Wang, T., Fu, P., and  
727 Huang, H.: Radiative and heterogeneous chemical effects of aerosols on ozone and inorganic  
728 aerosols over East Asia, *Science of The Total Environment*, 622-623, 1327-1342,  
729 10.1016/j.scitotenv.2017.12.041, 2018.

730 Li, J., Nagashima, T., Kong, L., Ge, B., Yamaji, K., Fu, J. S., Wang, X., Fan, Q., Itahashi, S., Lee,  
731 H. J., Kim, C. H., Lin, C. Y., Zhang, M., Tao, Z., Kajino, M., Liao, H., Li, M., Woo, J. H.,  
732 Kurokawa, J., Wang, Z., Wu, Q., Akimoto, H., Carmichael, G. R., and Wang, Z.: Model  
733 evaluation and intercomparison of surface-level ozone and relevant species in East Asia in the

734 context of MICS-Asia Phase III – Part 1: Overview, *Atmos. Chem. Phys.*, 19, 12993-13015,  
735 10.5194/acp-19-12993-2019, 2019.

736 Li, K., Jacob, D. J., Shen, L., Lu, X., De Smedt, I., and Liao, H.: Increases in surface ozone pollution  
737 in China from 2013 to 2019: anthropogenic and meteorological influences, *Atmos. Chem.*  
738 *Phys.*, 20, 11423-11433, 10.5194/acp-20-11423-2020, 2020.

739 Li, M., Liu, H., Geng, G., Hong, C., Liu, F., Song, Y., Tong, D., Zheng, B., Cui, H., Man, H., Zhang,  
740 Q., and He, K.: Anthropogenic emission inventories in China: a review, *National Science*  
741 *Review*, 4, 834-866, 10.1093/nsr/nwx150, 2017a.

742 Li, M., Zhang, Q., Kurokawa, J.-i., Woo, J.-H., He, K., Lu, Z., Ohara, T., Song, Y., Streets, D. G.,  
743 Carmichael, G. R., Cheng, Y., Hong, C., Huo, H., Jiang, X., Kang, S., Liu, F., Su, H., and Zheng,  
744 B.: MIX: a mosaic Asian anthropogenic emission inventory under the international  
745 collaboration framework of the MICS-Asia and HTAP, *Atmospheric Chemistry And Physics*,  
746 17, 935-963, 10.5194/acp-17-935-2017, 2017b.

747 Liu, H., Liu, Z., and Lu, F.: A Systematic Comparison of Particle Filter and EnKF in Assimilating  
748 Time-Averaged Observations, *Journal of Geophysical Research-Atmospheres*, 122, 13155-  
749 13173, 10.1002/2017jd026798, 2017.

750 Liu, Z., Wang, Y., Vrekoussis, M., Richter, A., Wittrock, F., Burrows, J. P., Shao, M., Chang, C.-C.,  
751 Liu, S.-C., Wang, H., and Chen, C.: Exploring the missing source of glyoxal (CHOCHO) over  
752 China, *Geophysical Research Letters*, 39, 10.1029/2012GL051645, 2012.

753 Marais, E. A., Jacob, D. J., Guenther, A., Chance, K., Kurosu, T. P., Murphy, J. G., Reeves, C. E.,  
754 and Pye, H. O. T.: Improved model of isoprene emissions in Africa using Ozone Monitoring  
755 Instrument (OMI) satellite observations of formaldehyde: implications for oxidants and  
756 particulate matter, *Atmos. Chem. Phys.*, 14, 7693-7703, 10.5194/acp-14-7693-2014, 2014.

757 Marsh, D. R., Mills, M. J., Kinnison, D. E., Lamarque, J.-F., Calvo, N., and Polvani, L. M.: Climate  
758 Change from 1850 to 2005 Simulated in CESM1(WACCM), *Journal of Climate*, 26, 7372-  
759 7391, 10.1175/JCLI-D-12-00558.1, 2013.

760 Mo, Z., Huang, S., Yuan, B., Pei, C., Song, Q., Qi, J., Wang, M., Wang, B., Wang, C., Li, M., Zhang,  
761 Q., and Shao, M.: Deriving emission fluxes of volatile organic compounds from tower  
762 observation in the Pearl River Delta, China, *Science of The Total Environment*, 741, 139763,  
763 10.1016/j.scitotenv.2020.139763, 2020.

764 Mu, M., Randerson, J. T., van der Werf, G. R., Giglio, L., Kasibhatla, P., Morton, D., Collatz, G. J.,  
765 DeFries, R. S., Hyer, E. J., Prins, E. M., Griffith, D. W. T., Wunch, D., Toon, G. C., Sherlock,  
766 V., and Wennberg, P. O.: Daily and 3-hourly variability in global fire emissions and  
767 consequences for atmospheric model predictions of carbon monoxide, *Journal of Geophysical*  
768 *Research-Atmospheres*, 116, 10.1029/2011jd016245, 2011.

769 Opacka, B., Müller, J.-F., Stavrakou, T., Miralles, D. G., Koppa, A., Pagán, B. R., Potosnak, M. J.,  
770 Seco, R., De Smedt, I., and Guenther, A. B.: Impact of Drought on Isoprene Fluxes Assessed  
771 Using Field Data, Satellite-Based GLEAM Soil Moisture and HCHO Observations from OMI,  
772 *Remote Sensing*, 14, 2021, 2022.

773 Palmer, P. I., Abbot, D. S., Fu, T.-M., Jacob, D. J., Chance, K., Kurosu, T. P., Guenther, A.,  
774 Wiedinmyer, C., Stanton, J. C., Pilling, M. J., Pressley, S. N., Lamb, B., and Sumner, A. L.:  
775 Quantifying the seasonal and interannual variability of North American isoprene emissions  
776 using satellite observations of the formaldehyde column, *Journal of Geophysical Research*:

Atmospheres, 111, 10.1029/2005JD006689, 2006.

Paulson, S. E., and Orlando, J. J.: The reactions of ozone with alkenes: An important source of HO<sub>x</sub> in the boundary layer, *Geophysical Research Letters*, 23, 3727-3730, 10.1029/96GL03477, 1996.

Pierce, T., Geron, C., Bender, L., Dennis, R., Tonnesen, G., and Guenther, A.: Influence of increased isoprene emissions on regional ozone modeling, *Journal of Geophysical Research: Atmospheres*, 103, 25611-25629, 10.1029/98JD01804, 1998.

Ren, J., Guo, F., and Xie, S.: Diagnosing ozone–NO<sub>x</sub>–VOC sensitivity and revealing causes of ozone increases in China based on 2013–2021 satellite retrievals, *Atmos. Chem. Phys.*, 22, 15035-15047, 10.5194/acp-22-15035-2022, 2022.

Seco, R., Holst, T., Davie-Martin, C. L., Simin, T., Guenther, A., Pirk, N., Rinne, J., and Rinnan, R.: Strong isoprene emission response to temperature in tundra vegetation, *Proceedings of the National Academy of Sciences*, 119, e2118014119, doi:10.1073/pnas.2118014119, 2022.

Skamarock, W. C., and Klemp, J. B.: A time-split nonhydrostatic atmospheric model for weather research and forecasting applications, *Journal Of Computational Physics*, 227, 3465-3485, 10.1016/j.jcp.2007.01.037, 2008.

Souri, A. H., Nowlan, C. R., González Abad, G., Zhu, L., Blake, D. R., Fried, A., Weinheimer, A. J., Wisthaler, A., Woo, J. H., Zhang, Q., Chan Miller, C. E., Liu, X., and Chance, K.: An inversion of NO<sub>x</sub> and non-methane volatile organic compound (NMVOC) emissions using satellite observations during the KORUS-AQ campaign and implications for surface ozone over East Asia, *Atmos. Chem. Phys.*, 20, 9837-9854, 10.5194/acp-20-9837-2020, 2020.

Souri, A. H., Chance, K., Bak, J., Nowlan, C. R., González Abad, G., Jung, Y., Wong, D. C., Mao, J., and Liu, X.: Unraveling pathways of elevated ozone induced by the 2020 lockdown in Europe by an observationally constrained regional model using TROPOMI, *Atmos. Chem. Phys.*, 21, 18227-18245, 10.5194/acp-21-18227-2021, 2021.

Su, W., Liu, C., Chan, K. L., Hu, Q., Liu, H., Ji, X., Zhu, Y., Liu, T., Zhang, C., Chen, Y., and Liu, J.: An improved TROPOMI tropospheric HCHO retrieval over China, *Atmos. Meas. Tech.*, 13, 6271-6292, 10.5194/amt-13-6271-2020, 2020.

Tang, X., Zhu, J., Wang, Z. F., and Gbaguidi, A.: Improvement of ozone forecast over Beijing based on ensemble Kalman filter with simultaneous adjustment of initial conditions and emissions, *Atmospheric Chemistry And Physics*, 11, 12901-12916, 10.5194/acp-11-12901-2011, 2011.

van der Werf, G. R., Randerson, J. T., Giglio, L., van Leeuwen, T. T., Chen, Y., Rogers, B. M., Mu, M., van Marle, M. J. E., Morton, D. C., Collatz, G. J., Yokelson, R. J., and Kasibhatla, P. S.: Global fire emissions estimates during 1997–2016, *Earth System Science Data*, 9, 697-720, 10.5194/essd-9-697-2017, 2017.

Vigouroux, C., Langerock, B., Bauer Aquino, C. A., Blumenstock, T., Cheng, Z., De Mazière, M., De Smedt, I., Grutter, M., Hannigan, J. W., Jones, N., Kivi, R., Loyola, D., Lutsch, E., Mahieu, E., Makarova, M., Metzger, J. M., Morino, I., Murata, I., Nagahama, T., Notholt, J., Ortega, I., Palm, M., Pinardi, G., Röhling, A., Smale, D., Stremme, W., Strong, K., Sussmann, R., Té, Y., van Roozendael, M., Wang, P., and Winkler, H.: TROPOMI–Sentinel-5 Precursor formaldehyde validation using an extensive network of ground-based Fourier-transform infrared stations, *Atmos. Meas. Tech.*, 13, 3751-3767, 10.5194/amt-13-3751-2020, 2020.

Wang, H., Lu, X., Seco, R., Stavrakou, T., Karl, T., Jiang, X., Gu, L., and Guenther, A. B.: Modeling

820 Isoprene Emission Response to Drought and Heatwaves Within MEGAN Using  
821 Evapotranspiration Data and by Coupling With the Community Land Model, *Journal of*  
822 *Advances in Modeling Earth Systems*, 14, e2022MS003174, 10.1029/2022MS003174, 2022.

823 Wang, H., Yan, R., Xu, T., Wang, Y., Wang, Q., Zhang, T., An, J., Huang, C., Gao, Y., Gao, Y., Li,  
824 X., Yu, C., Jing, S., Qiao, L., Lou, S., Tao, S., and Li, Y.: Observation Constrained Aromatic  
825 Emissions in Shanghai, China, *Journal of Geophysical Research: Atmospheres*, 125,  
826 e2019JD031815, 10.1029/2019JD031815, 2020.

827 Wang, H., Wu, Q., Guenther, A. B., Yang, X., Wang, L., Xiao, T., Li, J., Feng, J., Xu, Q., and Cheng,  
828 H.: A long-term estimation of biogenic volatile organic compound (BVOC) emission in China  
829 from 2001–2016: the roles of land cover change and climate variability, *Atmos. Chem. Phys.*,  
830 21, 4825-4848, 10.5194/acp-21-4825-2021, 2021a.

831 Wang, J., Yan, R., Wu, G., Liu, Y., Wang, M., Zeng, N., Jiang, F., Wang, H., He, W., Wu, M., Ju, W.,  
832 and Chen, J. M.: Unprecedented decline in photosynthesis caused by summer 2022 record-  
833 breaking compound drought-heatwave over Yangtze River Basin, *Science Bulletin*, 68, 2160-  
834 2163, 10.1016/j.scib.2023.08.011, 2023.

835 Wang, N., Lyu, X., Deng, X., Huang, X., Jiang, F., and Ding, A.: Aggravating O<sub>3</sub> pollution due to  
836 NO<sub>x</sub> emission control in eastern China, *Science of The Total Environment*, 677, 732-744,  
837 10.1016/j.scitotenv.2019.04.388, 2019.

838 Wang, P., Liu, Y., Dai, J., Fu, X., Wang, X., Guenther, A., and Wang, T.: Isoprene Emissions  
839 Response to Drought and the Impacts on Ozone and SOA in China, *Journal of Geophysical  
840 Research: Atmospheres*, 126, e2020JD033263, 10.1029/2020JD033263, 2021b.

841 Wang, W., van der A, R., Ding, J., van Weele, M., and Cheng, T.: Spatial and temporal changes of  
842 the ozone sensitivity in China based on satellite and ground-based observations, *Atmos. Chem.  
843 Phys.*, 21, 7253-7269, 10.5194/acp-21-7253-2021, 2021c.

844 Warneke, C., de Gouw, J. A., Del Negro, L., Brioude, J., McKeen, S., Stark, H., Kuster, W. C.,  
845 Goldan, P. D., Trainer, M., Fehsenfeld, F. C., Wiedinmyer, C., Guenther, A. B., Hansel, A.,  
846 Wisthaler, A., Atlas, E., Holloway, J. S., Ryerson, T. B., Peischl, J., Huey, L. G., and Hanks, A.  
847 T. C.: Biogenic emission measurement and inventories determination of biogenic emissions in  
848 the eastern United States and Texas and comparison with biogenic emission inventories,  
849 *Journal of Geophysical Research: Atmospheres*, 115, 10.1029/2009JD012445, 2010.

850 Whitaker, J. S., and Hamill, T. M.: Ensemble data assimilation without perturbed observations,  
851 *Monthly Weather Review*, 130, 1913-1924, 10.1175/1520-  
852 0493(2002)130<1913:Edawpo>2.0.Co;2, 2002.

853 Wolfe, G. M., Kaiser, J., Hanisco, T. F., Keutsch, F. N., de Gouw, J. A., Gilman, J. B., Graus, M.,  
854 Hatch, C. D., Holloway, J., Horowitz, L. W., Lee, B. H., Lerner, B. M., Lopez-Hilfiker, F.,  
855 Mao, J., Marvin, M. R., Peischl, J., Pollack, I. B., Roberts, J. M., Ryerson, T. B., Thornton, J.  
856 A., Veres, P. R., and Warneke, C.: Formaldehyde production from isoprene oxidation  
857 across NO<sub>x</sub> regimes, *Atmos. Chem. Phys.*, 16, 2597-2610, 10.5194/acp-16-2597-2016, 2016.

858 Yuan, B., Kaser, L., Karl, T., Graus, M., Peischl, J., Campos, T. L., Shertz, S., Apel, E. C., Hornbrook,  
859 R. S., Hills, A., Gilman, J. B., Lerner, B. M., Warneke, C., Flocke, F. M., Ryerson, T. B.,  
860 Guenther, A. B., and de Gouw, J. A.: Airborne flux measurements of methane and volatile  
861 organic compounds over the Haynesville and Marcellus shale gas production regions, *Journal  
862 of Geophysical Research: Atmospheres*, 120, 6271-6289, 10.1002/2015JD023242, 2015.

863 Zhang, M., Zhao, C., Yang, Y., Du, Q., Shen, Y., Lin, S., Gu, D., Su, W., and Liu, C.: Modeling  
864 sensitivities of BVOCs to different versions of MEGAN emission schemes in WRF-Chem  
865 (v3.6) and its impacts over eastern China, *Geosci. Model Dev.*, 14, 6155-6175, 10.5194/gmd-  
866 14-6155-2021, 2021.

867 Zhang, Q., Streets, D. G., Carmichael, G. R., He, K. B., Huo, H., Kannari, A., Klimont, Z., Park, I.  
868 S., Reddy, S., Fu, J. S., Chen, D., Duan, L., Lei, Y., Wang, L. T., and Yao, Z. L.: Asian emissions  
869 in 2006 for the NASA INTEX-B mission, *Atmos. Chem. Phys.*, 9, 5131-5153, 10.5194/acp-9-  
870 5131-2009, 2009.

871 Zheng, B., Tong, D., Li, M., Liu, F., Hong, C., Geng, G., Li, H., Li, X., Peng, L., Qi, J., Yan, L.,  
872 Zhang, Y., Zhao, H., Zheng, Y., He, K., and Zhang, Q.: Trends in China's anthropogenic  
873 emissions since 2010 as the consequence of clean air actions, *Atmospheric Chemistry And*  
874 *Physics*, 18, 14095-14111, 10.5194/acp-18-14095-2018, 2018.

875 Zhou, B., Guo, H., Zeren, Y., Wang, Y., Lyu, X., Wang, B., and Wang, H.: An Observational  
876 Constraint of VOC Emissions for Air Quality Modeling Study in the Pearl River Delta Region,  
877 *Journal of Geophysical Research: Atmospheres*, 128, e2022JD038122,  
878 10.1029/2022JD038122, 2023.

879